Chem

CellPress

Research Article

Carrier Dynamics Engineering for High-Performance Electron-Transport-Layer-Free Perovskite Photovoltaics

Qiwei Han[1,2,3,6], Jie Ding[1,4,6], Yusong Bai[3], Tianyang Li[2,3], Jing-Yuan Ma[1,4], Yao-Xuan Chen[1,4], Yihao Zhou[2], Jie Liu[1,4], Qian-Qing Ge[1,4], Jie Chen[4], Jeffrey T. Glass[2,5], Michael J. Therien[3], Jie Liu[3]*, David B. Mitzi[2,3]* and Jin-Song Hu[1,4,7]*

[1]CAS Key Laboratory of Molecular Nanostructure and Nanotechnology, CAS Research/Education Center for Excellence in Molecular Sciences, Institute of Chemistry, Chinese Academy of Sciences, Beijing 100190, China.
[2]Department of Mechanical Engineering and Materials Science, Duke University, Durham, NC 27708, USA.
[3]Department of Chemistry, Duke University, Durham, NC 27708, USA.
[4]School of Chemical Sciences, University of Chinese Academy of Sciences, Beijing 100049, China.
[5]Department of Electrical and Computer Engineering, Duke University, Durham, NC 27708, USA.
[6]These authors contributed equally to this work.
[7]Lead Contact.
*Correspondence: hujs@iccas.ac.cn; david.mitzi@duke.edu; j.liu@duke.edu.

SUMMARY

Electron-transport-layer-free (ETL-free) device architectures are promising designs for perovskite photovoltaics (PV), offering simpler configurations, low cost and convenience for versatile optoelectronics. However, the development of the ETL-free PV is hindered by their low performance. Herein, we reveal that low electron-injection rate at the ETL-free interface is responsible for the performance loss. Moreover, we demonstrate that improving carrier lifetimes in the perovskite films can remedy the poor carrier extraction at the interfaces, enabling carrier collection efficiency in ETL-free PV to approach that in ETL-containing devices. Using perovskite films with microsecond carrier lifetimes, ETL-free PV devices are obtained with power conversion efficiency (*PCE*) of 19.5%, nearly-eliminated hysteresis and good stability. Such a PCE value is comparable to that (20.7%) of the analogous ETL-containing devices. These results offer new opportunities for ETL-free architecture designs in the perovskite PV family. More importantly, this research provides a general approach to improve the performance of PV with low-injection-rate interfaces.

INTRODUCTION

Perovskite photovoltaics (PV) has attracted tremendous attention due to recent advances in power conversion efficiency (*PCE*) and diverse processing options.[1-8] Other than high performance, factors including good stability, simpler device configuration and low processing cost should be considered in next-generation perovskite PV. Currently, high-performance perovskite solar cells exclusively employ p-i-n device architectures,[5-7] wherein distinct electron transport (n-type) and hole transport (p-type) layers are generally viewed as critical components for reliable photogenerated carrier extraction.[9] However, the deposition processes to construct a p-i-n architecture, especially for inorganic electron-transport layers (ETLs), typically require high-temperature conditions (e.g., ~500 °C for TiO_2, ~500 °C for $BaSnO_3$, and ~250 °C for ZnO).[7; 10-12] Such high temperature steps compromise the low-cost advantage of solution-based approaches for perovskite film deposition (e.g., generally performed at 25~100 °C), leading, for example, to increased projected payback time for perovskite PV and other optoelectronics.[13] Additionally, in building more complex optoelectronic devices, such as all-perovskite tandem solar cells, the high temperatures to process ETLs in top cells can damage the perovskite and/or other temperature-sensitive films in bottom cells. The high temperatures can also melt prospective flexible substrates and/or cause ion migration from substrates, limiting the applications of perovskite technology in versatile optoelectronics. More importantly, the existence of some ETLs themselves can detrimentally impact the perovskite devices.[14-17] For example, ZnO ETLs can cause the

decomposition of perovskite layers during annealing[15] and TiO_2 ETLs can induce degradation of perovskite films under illumination.[16] Regardless of these performance issues, the inclusion of numerous layers in devices is not desired for effective commercialization. In short, these ETL-induced issues lead to prospects of lower processing yields, increased payback times, faster degradation and difficulties in constructing more versatile/complex perovskite optoelectronics. To address these issues, building solar cells without distinct ETLs in the architectures is a promising direction for next-generation perovskite PV. In fact, studies have demonstrated that perovskite films possess superior properties for charge-carrier dissociation[18] and transport,[19; 20] and that the transparent electrodes (e.g., fluorine-doped tin oxide glass (FTO) and tin-doped indium oxide glass (ITO)) themselves are typically n-type semiconductors. Therefore, distinct ETLs should not theoretically be necessary for high-performance perovskite PV. Unfortunately, all current-generation ETL-free perovskite solar cells suffer from low *PCE*, with relatively large hysteresis and inferior stability.[21-29] In this regard, creating deeper understanding and developing effective approaches to improve the performance are keys for the success of ETL-free perovskite PV.

In this work, we reveal that the carrier injection process is significantly inhibited at the interface in the absence of an ETL, which leads to insufficient carrier collection and severe interfacial carrier recombination. The recombination decreases the external quantum efficiency (EQE) in both short- and long-wavelength ranges and thereby compromises the performance for ETL-free perovskite PV. Moreover, we demonstrate that improving the intrinsic carrier lifetimes in perovskite films can counterbalance the inferior device interfaces and suppress the carrier recombination at the ETL-free interface. Through such carrier-dynamics engineering, the carrier collection efficiency in the ETL-free perovskite PV can be remarkably tailored to approach that in ETL-containing devices. Benefiting from this discovery, we exploit perovskite films with microsecond carrier lifetimes to successfully realize ETL-free perovskite PV with best *PCE* of 19.52% (18.48% in average), nearly eliminated hysteresis and good stability. Such a high *PCE* is comparable to the value (20.7%) achieved for ETL-containing solar cells prepared using analogous perovskite films. Our research provides insight into ETL-free solar cells and points out a promising direction for perovskite PV and analogous optoelectronic devices, offering simultaneously high performance, simplified processing and better prospects for ultra-low-cost device fabrication.

RESULTS and DISCUSSION

ETL-Free and ETL-Containing PV

To identify the difference between typical ETL-free and ETL-containing PV, pristine $CH_3NH_3PbI_3$ ($MAPbI_3$) perovskite films are used as absorbers. The pristine $MAPbI_3$ films are deposited by a one-step method, using a precursor solution containing a 1:1 molar ratio of MAI and PbI_2. ITO-coated glass is used as the transparent electrode substrate. In the ETL-containing PV devices, SnO_2 is chosen as the ETL due to the wider bandgap of SnO_2 (e.g., compared to TiO_2), such that the distinct ETL would at most minimally impact the light absorption within the perovskite films during device operation (as discussed later).[30] The full details for film deposition are described in the Methods section. Top-view scanning electron microscope (SEM) images in Figure 1A and Figure 1B present the morphologies of typical pristine $MAPbI_3$ films on glass/ITO and glass/ITO/SnO_2 substrates, respectively, from which one can deduce that the $MAPbI_3$ films share similar film morphologies and compactness on both substrates. From X-ray diffraction (XRD) patterns (Figure S1), the $MAPbI_3$ films exhibit similar structural properties on both substrates. The optical absorption spectra (Figure S2) illustrate that the $MAPbI_3$ films also have similar optical features (E_g = ~1.60 eV). These results indicate that glass/ITO and glass/ITO/SnO_2 substrates do not impact the basic structural/optical properties of $MAPbI_3$ films. In many respects, this observation is not surprising, given that both SnO_2 and ITO present a tin-oxide-based surface.

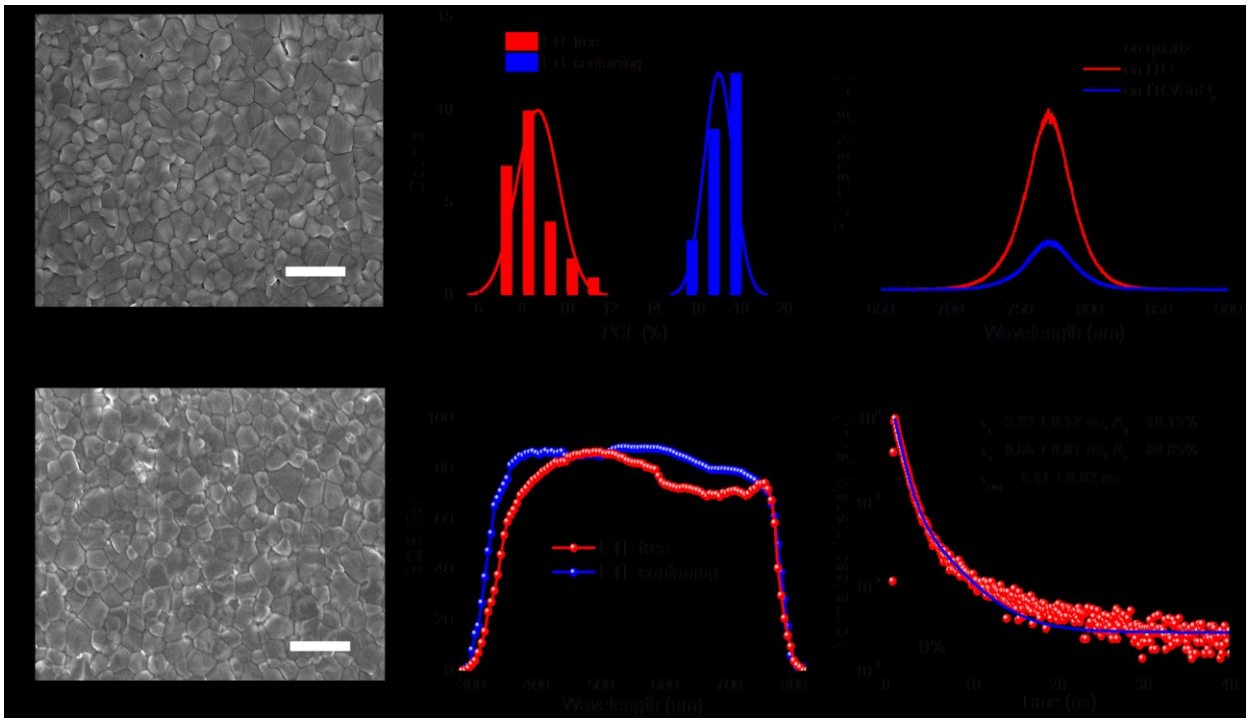

Figure 1. ETL-free and ETL-containing PV using pristine $MAPbI_3$

(A) Top-view SEM image of a pristine $MAPbI_3$ film deposited on glass/ITO substrate.

(B) Top-view SEM image of a pristine $MAPbI_3$ film deposited on glass/ITO/SnO_2 substrate. Both SEM images employ a 1 μm scale bar.

(C) *PCE* distributions for ETL-free and ETL-containing PV, respectively.

(D) EQE spectra for the ETL-free and ETL-containing PV, respectively.

(E) The steady-state PL spectra of pristine $MAPbI_3$ films deposited on quartz, glass/ITO and glass/ITO/SnO_2 substrates, respectively.

(F) The TRPL spectrum of a pristine $MAPbI_3$ films deposited on quartz substrate. The average carrier lifetime (τ_{avg}) is obtained by considering the long-lived component (τ_1) and short-lived component (τ_2) and their corresponding amplitudes (A_1 and A_2).

To examine the PV performance for such $MAPbI_3$ films in devices, ETL-free and ETL-containing perovskite PV devices were fabricated with the device architectures of glass/ITO/$MAPbI_3$/2,2',7,7'-tetrakis[N,N-di(4-methoxyphenyl)amino]-9,9'-spirobifluorene (Spiro-OMeTAD)/Au and glass/ITO/SnO_2/$MAPbI_3$/Spiro-OMeTAD/Au, respectively. Figure 1C presents the statistical distributions of *PCE* values, from which the ETL-free devices yield *PCE* from 7.70% to 11.40% (8.68 % in average) for 24 devices, while ETL-containing devices yield *PCE* from 15.78% to 17.99% (16.97% % in average) for 24 devices. The statistical results indicate that the *PCE* of a typical ETL-free PV device is significantly lower than the analogous value for a typical ETL-containing device when using the pristine $MAPbI_3$ films, which is consistent with earlier reports.[21; 22] To figure out the reasons for the compromised *PCE*, the EQE was compared for ETL-free and ETL-containing perovskite PV.

From the EQE spectra (Figure 1D), the EQE response of the ETL-free device falls significantly lower than that for the analogous ETL-containing device, especially in the short (300-400 nm) and long (500-750 nm) wavelength ranges. Such results indicate that the carrier collection is less effective in ETL-fee devices (e.g., due to enhanced recombination in the ETL-free device structures). Since the glass/ITO and glass/ITO/SnO_2 substrates have nearly the same optical absorption features (Figure S3) and the perovskite films have similar grain structures, the reduced carrier collection in ETL-free devices likely derives from the different interface. Previous study attributed this device performance loss to the lack of efficient hole blocking.[22] From this opinion, due the absence of a distinct ETL, photogenerated holes can easily reach the ITO/$MAPbI_3$ interface and ITO contains the high density of electrons which would make photogenerated holes recombine with the electrons from ITO, eventually leading to the loss of photogenerated carriers and device performance.

However, study showed that work function of ITO (-4.7 eV) is higher than the Fermi level of $MAPbI_3$.[31] Therefore, The band bending direction of $MAPbI_3$ films at the ITO/$MAPbI_3$ interface

is downward and the built-in electric field formed at the interface points from ITO to $MAPbI_3$ film which attracts electrons and repel holes photogenerated in $MAPbI_3$ films (shown in Figure S4). In addition, ITO is a typical n-type semiconductor whose valence band maximum edge is lower than that of perovskite materials. Such situations make the as-formed ITO/$MAPbI_3$ interface is preferable for electron extracting and hole blocking. Based on the analysis, the performance loss in ETL-free perovskite PV may not be due to the lack of hole blocking.

To understand the impact of ITO/$MAPbI_3$ interface on photogenerated carriers, photoluminescence (PL) quenching measurements were performed. Figure 1E presents the steady-state PL spectra for the $MAPbI_3$ films on quartz, glass/ITO and glass/ITO/SnO_2, respectively, from which we can observe that the PL signal quenches less on the ETL-free substrates. The quenching results evidently illustrate that the interfacial carrier injection process is substantially inhibited without the assistance of a distinct ETL, which suggests that the compromised performance of ETL-free perovskite PV originates from the inhibited carrier injection on ITO substrate. Study indicated that the work function/Fermi level of SnO_2 is around -4.36 eV which is higher than the work function of ITO.[30] Without SnO_2 ETL in the devices, the interfacial built-in electric field may become weaker due to relatively lower work function of ITO. The inhibited injection could be derived from this weaker built-in electric field.

At/near the interface, if the carriers photogenerated in perovskite films cannot be rapidly collected, these carriers will undergo recombination (e.g., radiative and/or nonradiative recombination) in the perovskite films. From the TRPL result (Figure 1F), the pristine $MAPbI_3$ films used in typical ETL-free PV exhibit short average carrier lifetimes (τ_{avg} = 1.17 $\pm$ 0.02 ns). We refer to such lifetimes as "intrinsic" lifetimes since they are measured for films on quartz substrates rather than for films within device structures, wherein built-in electric fields will impact the values measured. The photogenerated carriers with such short intrinsic lifetimes will more readily recombine at/near the interface if built-in electric field cannot drift them to the interface and rapidly across the interface to the contact.
For reducing the carrier recombination near the low-injection-rate interface, the typical approach involves adding an additional layer at this poor interface to provide a strong built-in electric field to fast drift the carriers cross the interface for extraction (ultimately, before recombination). However, this approach adds extra layers to the ETL-free architectures and creates an architecture that is essentially identical to that for the ETL-containing devices. Logically, if we are not able to improve the interfacial band alignment to enhance carrier drifting, then the next best thing would be to improve the carrier lifetimes within the perovskite films, so that the photogenerated carriers can survive long enough to diffuse to the interface and make it across the less effective interface. Based on this analysis and expectation, increase of the lifetimes for the carrier diffusion could be an effective method to compensate the weaker "drifting ability" (e.g., built-in electric field), which is highly desired for ETL-free PV (even more so than in ETL-containing PV). In the following section, we will explore the effect of carrier lifetimes on the performance of ETL-free PV devices.

Impact of Carrier Lifetimes on PV Performance

The effect of the intrinsic carrier lifetime on the performance of ETL-free perovskite PV was explored by introducing extra PbI_2 into the $MAPbI_3$ films to tune the film carrier lifetimes.[10; 13] Top-view SEM images (Figure S5) show that the $MAPbI_3$ films with 2.5%, 5.0% and 7.5% extra PbI_2 on glass/ITO substrates have similar grain size to that in the pristine $MAPbI_3$ film as shown in Figure 1A. From the atomic force microscope (AFM) images in Figure S6, the $MAPbI_3$ films share similar surface roughness, within the range of 6 to 8 nm, illustrating that adding extra PbI_2 to the $MAPbI_3$ films does not significantly impact film morphology. The optical absorption spectra for the $MAPbI_3$ films with 0~7.5% extra PbI_2 (Figure S7) indicate that adding extra PbI_2 does not remarkably affect the absorption characteristics of the $MAPbI_3$ films (over the limited range of PbI_2 added).

TRPL was performed for the $MAPbI_3$ films on quartz substrates to evaluate the optoelectronic properties of the $MAPbI_3$ films with extra PbI_2. By comparing the TRPL spectra in Figure 2A and Figure 1F, it can be observed that adding extra PbI_2 significantly enhances the intrinsic carrier lifetimes of the $MAPbI_3$ films, from several nanoseconds to several hundred nanoseconds. To further pursue this point, steady-state PL measurements were also

performed on the $MAPbI_3$ films (Figure 2B), showing significant intensity enhancement with extra PbI_2 addition, which is consistent with the TRPL results. In addition to the intrinsic carrier lifetimes, we also measured the steady-state PL for the $MAPbI_3$ films with extra PbI_2 on glass/ITO substrates, to understand whether extra PbI_2 in $MAPbI_3$ films may change the carrier injection rate at the ITO/$MAPbI_3$ interface (as shown in Figure S8). Since the PL intensity of the $MAPbI_3$ films significantly varies with PbI_2 levels, we define a PL quenching rate metric (QR_{PL})—i.e., $QR_{PL} = (I_1-I_2)/I_1$, where I_1 is the PL intensity of the $MAPbI_3$ film on quartz, while I_2 is the analogous value on ITO—to better evaluate the carrier injection at the ITO/perovskite interface. By comparing the QR_{PL} values (Figure S9), it is seen that the extra PbI_2 itself in $MAPbI_3$ films does not enhance carrier injection yield at the ITO/perovskite interface, as underscored by the extent of PL quenching. This result is reasonable since the relative conduction band position of PbI_2 is higher than that of perovskite materials so that the extra PbI_2 accumulation at the ITO/$MAPbI_3$ interface would not improve the band alignment for electron injection.[32] Taken together, the TRPL and PL results indicate that addition of extra PbI_2 significantly improves the carrier lifetimes in the $MAPbI_3$ films but does not facilitate the electron injection at the ITO/$MAPbI_3$ interface.[10; 13]

To show the correlation between the intrinsic carrier lifetimes and performance for ETL-free perovskite PV, solar cells using extra-PbI_2-added $MAPbI_3$ films were fabricated with the same ETL-free architecture (glass/ITO/$MAPbI_3$/Spiro-OMeTAD/Au) described above. For each PbI_2 addition level, 24 devices are used for the statistical results shown in Figure 2C and Figure S10. It can be observed that the trend of all the PV parameters is similar to the trend of carrier lifetimes as the PbI_2 addition level changes, illustrating close correlation between the device performances and the intrinsic carrier lifetimes and that long carrier lifetimes substantially benefit the ETL-free device performance. For comparison, ETL-containing PV devices were also fabricated. From the *PCE* distributions shown in Figure S11, the intrinsic carrier lifetimes are also seen to affect the performance of ETL-containing PV. To explore the degree to which the carrier lifetimes can impact on the ETL-free and ETL-containing perovskite solar cells, respectively, the correlations between extra PbI_2 addition levels and average *PCE* values are presented. From Figure 2D and Figure S12, it is found that the performance of ETL-free devices is substantially more sensitive to the intrinsic carrier lifetimes relative to ETL-containing PV.

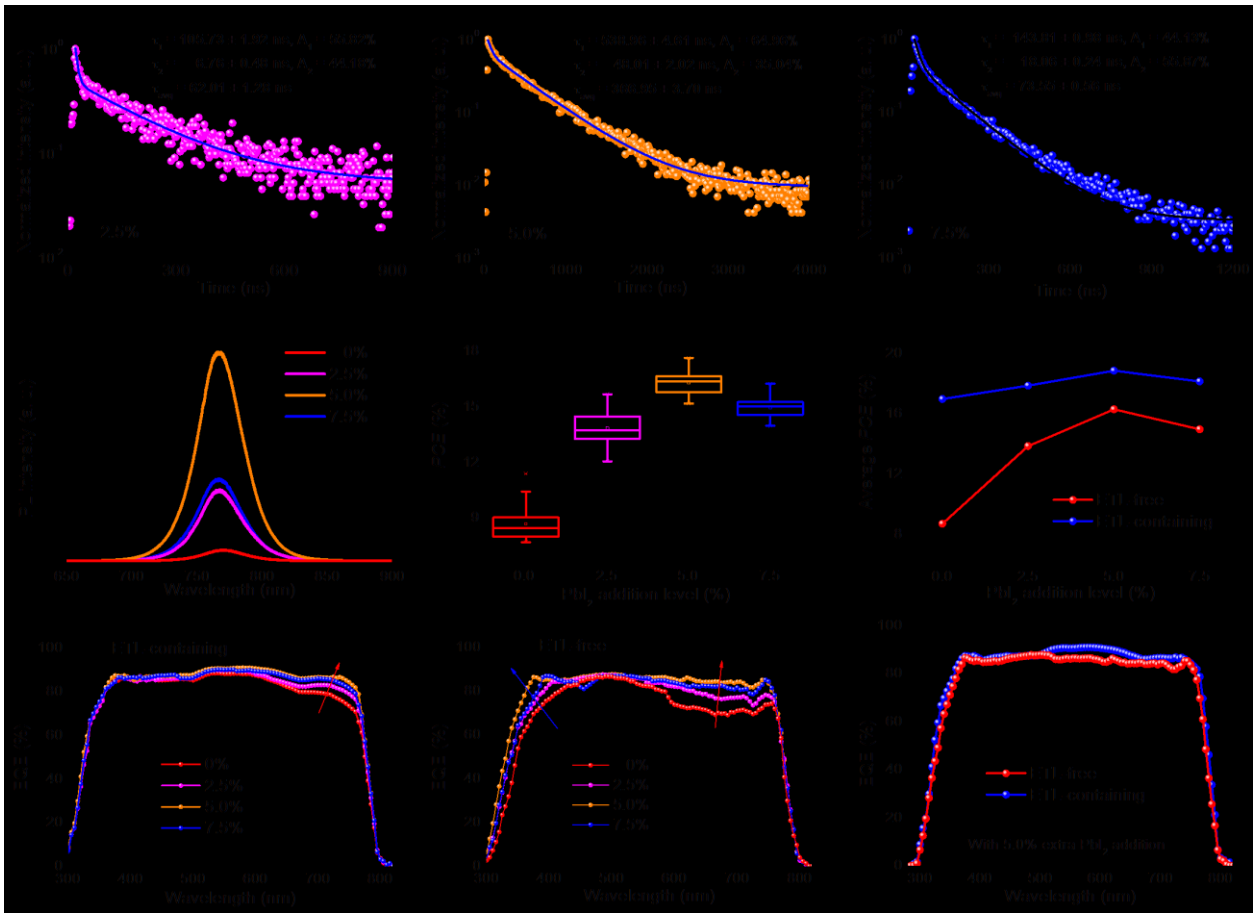

Figure 2. Correlations between carrier lifetimes and PV properties

(A) The TRPL spectra of $MAPbI_3$ films with addition of 2.5~7.5% extra PbI_2.

(B) The steady-state PL spectra of $MAPbI_3$ films with addition of 0~7.5% extra PbI_2. The $MAPbI_3$ films for TRPL and PL were deposited on quartz substrates.

(C) *PCE* distributions for ETL-free PV by using $MAPbI_3$ films with addition of 0~7.5% extra PbI_2. The corresponding distributions of the V_{oc}, J_{sc} and *FF* are shown in Figure S10.

(D) The correlations between PbI_2 addition level in $MAPbI_3$ films and average *PCE* values for ETL-free and ETL-containing solar cells. The correlations for other photovoltaics parameters are shown in Figure S12.

(E) EQE spectra of the ETL-containing PV by using $MAPbI_3$ films with addition of 0~7.5% extra PbI_2.

(F) EQE spectra of the ETL-free PV by using $MAPbI_3$ films with addition of 0~7.5% extra PbI_2.

(G) EQE spectra of the ETL-free and ETL-containing PV by using $MAPbI_3$ films with addition of 5% extra PbI_2.

The EQE was also measured on the ETL-containing and ETL-free PV devices (Figure 2E and Figure 2F), for better understanding the impact of carrier lifetimes on photogenerated carrier collection. It can be observed that as carrier lifetimes increase, both the short- and long-wavelength spectral responses substantially improve for ETL-free PV, while only the long-wavelength range increases for ETL-containing PV. For ETL-containing PV (Figure 2E), the EQE increase in the long-wavelength range can be attributed to the reduction of bulk-defect-induced recombination, enabling more long-wavelength-excited carriers to travel through the perovskite films for extraction. For ETL-free devices (Figure 2F), the additional enhancement of short-wavelength EQE could be due to reduced carrier recombination at the ETL-free interface, leading to increasing numbers of short-wavelength-excited carriers being effectively collected at the ITO/perovskite interface. The EQE spectra explain the result that the performance of ETL-free PV is more sensitive to carrier lifetimes. Moreover, comparing the EQE spectra shown in Figure 2G, we see that the EQE values for the ETL-free PV progressively converge to that for ETL-containing PV for long carrier lifetimes, totally different from the situation for short carrier lifetimes (Figure 1D). Long carrier lifetimes in perovskite films therefore appear to be important for obtaining high-performance ETL-free PV. In addition, these results also suggest that use of distinct ETLs is beneficial for the device performance if the intrinsic carrier lifetimes in the associated perovskite absorbers are relatively short.

Perovskite Film with Microsecond Carrier Lifetimes

For further boosting the *PCE* of ETL-free PV, mixed-cation lead mixed-halide perovskite films ($Cs_{0.05}FA_{0.8}MA_{0.15}PbI_{2.55}Br_{0.45}$, referred to as CsFAMA, where FA = formamidinium) with microsecond carrier lifetimes were used as the light absorbers in devices (see the Methods section for deposition details).[33] The top-view SEM image of a CsFAMA film on glass/ITO substrate (Figure 3A) reveals that the grain size is ~500 nm, with good compactness and coverage over relatively large area (Figure S13). Based on the AFM image (Figure S14), the CsFAMA films exhibit flat surfaces, with roughness on the order of 20 nm. The relatively flat surface reduces the contact area at the CsFAMA/Spiro-OMeTAD interface, leading to reduced interfacial recombination and therefore benefiting the device performance.

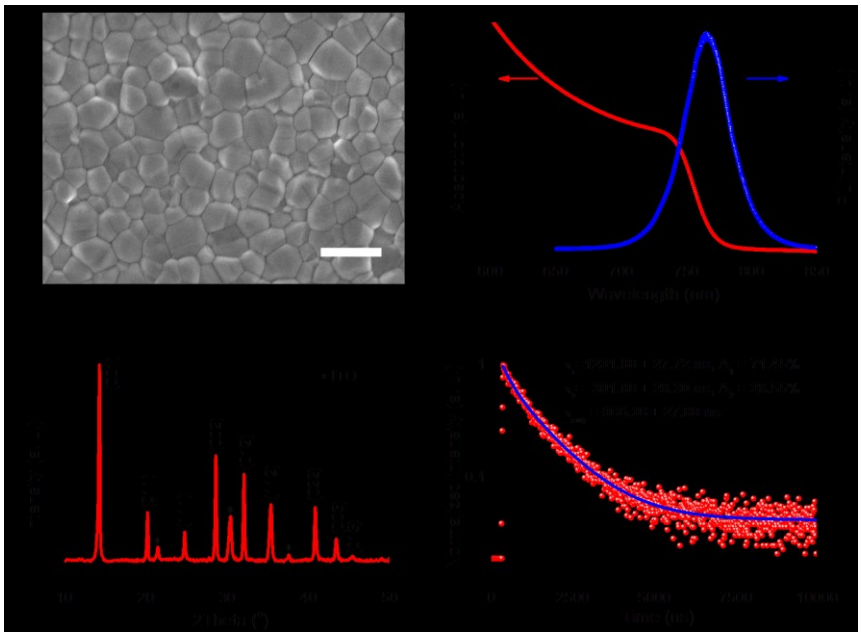

Figure 3. Characterization of CsFAMA perovskite film

(A) Top-view SEM image of a CsFAMA perovskite film. The scale bar is 1 μm.

(B) The XRD pattern of a CsFAMA perovskite film.

(C) The optical absorption spectrum and PL spectrum of a CsFAMA perovskite film.

(D) The TRPL spectrum of a CsFAMA perovskite film. The film for SEM, optical absorption and XRD measurements was deposited on glass/ITO substrates. The film for PL and TRPL measurements was deposited on quartz substrates.

The XRD pattern (Figure 3B) for a CsFAMA film on glass/ITO substrate demonstrates that the CsFAMA film contains only the photoactive perovskite α-phase (black phase), and no non-perovskite δ-phase (yellow phase) exists to negatively impact the optoelectronic properties. To evaluate the optical properties of the CsFAMA film, optical absorption and steady-state PL measurements were performed (Figure 3C) and demonstrate that the optical absorption onset and PL peak are consistent (E_g = ~1.59 eV shown in Figure S15). To understand the charge carrier dynamics, TRPL data was acquired for a CsFAMA film on quartz substrate. The intrinsic charge carrier lifetimes extracted from the PL dynamics (Figure 3D) are τ_1 = 1231.9 ± 27.7 ns and τ_2 = 301.9 ± 28.3 ns; these values have respective amplitudes A_1 = 71.4% and A_2 = 28.6% (τ_{avg} is 966.4 ± 27.9 ns). Such microsecond carrier lifetimes approximately three times the value achieved for the previously shown $MAPbI_3$ film with 5% extra PbI_2 added, are expected to substantially boost the performance of ETL-free perovskite PV, as discussed above.

High-Performance ETL-Free Devices

Given the above results, ETL-free perovskite solar cells were fabricated with the device architecture ITO/CsFAMA/Spiro-OMeTAD/Au. From the SEM image of device cross-section (Figure 4A), the thicknesses of the CsFAMA, Spiro-OMeTAD and Au layers are seen to be ~ 650 nm, ~150 nm and ~80 nm, respectively. The statistical distributions of *PCE* values (reverse

scanning direction) for 24 ETL-free devices (Figure 4B) vary from 17.85 to 19.52% (18.48% in average). For comparison, analogous ETL-containing perovskite solar cells with an ITO/SnO_2/CsFAMA/Spiro-OMeTAD/Au structure yield similar performance levels (Figure 4B), with *PCE* values varying from 19.60 to 20.72% (20.03% average). To evaluate the hysteresis behavior, the best-performing devices were measured using both forward and reverse voltage scanning directions. From the reverse (forward) scan, the best-performing ETL-free device (Figure 4C) yields *PCE* of 19.52 (18.84) %, open-circuit voltage (V_{oc}) of 1.061 (1.069) V, shirt-circuit current density (J_{sc}) of 23.61 (23.39) mA cm^{-2} and fill factor (*FF*) of 77.79 (75.37) %. The best-performing ETL-containing device (Figure S16) yields *PCE* of 20.72 (20.51) %, V_{oc} of 1.100 (1.100) V, J_{sc} of 23.75 (23.51) mA cm^{-2} and *FF* of 79.28 (79.23) %. We can see that the ETL-free device hysteresis approaches that of the ETL-containing device.

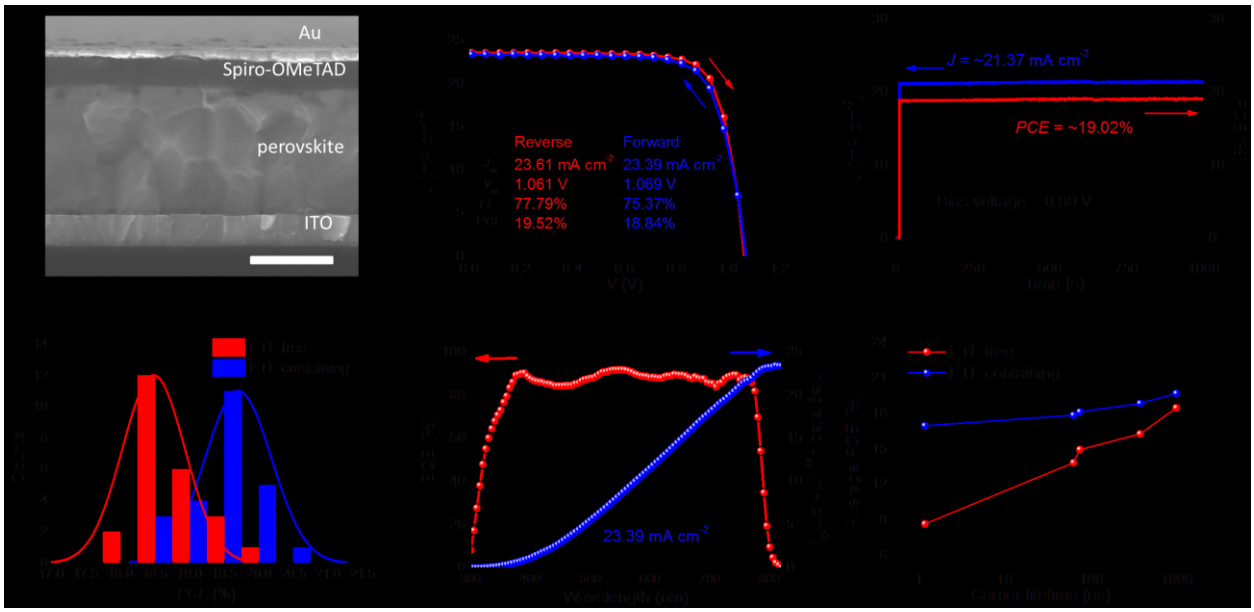

Figure 4. Device architecture and performance for ETL-free perovskite photovoltaics

(A) Cross-section SEM image of an ETL-free perovskite solar cell with device architecture glass/ITO/CsFAMA/Spiro-OMeTAD/Au. The image employs a 500 nm scale bar.

(B) *PCE* distributions for ETL-free and ETL-containing perovskite solar cells prepared with CsFAMA films.

(C) *J-V* characteristics of the best-performing ETL-free perovskite solar cell prepared with a CsFAMA film. *J-V* characteristics are evaluated with reverse and forward voltage scanning directions.

(D) EQE and integrated J_{sc} of the best-performing ETL-free perovskite solar cell with a CsFAMA film.

(E) Steady-state output profile for the best-performing ETL-free perovskite solar cell, prepared using a CsFAMA film, under a bias voltage of 0.89 V.

(F) correlations between carrier lifetimes of perovskite films and average *PCE* for ETL-free and ETL-containing perovskite photovoltaics, respectively.

The EQE spectrum of the best-performing ETL-free device (Figure 4D) illustrates high quantum efficiency for energies above the band gap, leading to an integrated J_{sc} of 23.39 mA cm^{-2}, which is consistent with the results from the *J-V* characteristics. The steady-state output profile (Figure 4E) shows that the best performing ETL-free device has a steady-state output current density (*J*) of ~21.37 mA cm^{-2} under 0.89 V applied bias, corresponding to a stabilized *PCE* value of ~19.02%—i.e., showing good agreement with the *J-V* measurement. Such performance level for the ETL-free devices approach record metrics for any type of perovskite devices and represent the best *PCE* performance level among all currently reported ETL-free perovskite solar cells to date.

Finally, the correlations between carrier lifetimes and device performance are examined for ETL-free/ETL-containing PV (Figure 4F). Such results indicate that the *PCE* discrepancy between ETL-free and ETL-containing perovskite solar cells is significantly reduced as the carrier lifetime increases, and further suggest that extending the carrier lifetimes of perovskite films (e.g., >>1 μs) may boost the *PCE* of associated ETL-free perovskite solar cells to the same level as ETL-containing perovskite solar cells. Moreover, the *PCE* of the best-performing ETL-free device remains ~19.1% (from *J-V* measurement) after 1000 hours of storage (temperature of ~25 °C and relative humidity of ~25% in the dark), illustrating that

the ETL-free devices have good environmental stability (Figure S17). The photo-stability of the best-performing ETL-free perovskite solar cells was also measured using continuous light soaking (one sun) under ambient conditions (temperature of ~25 °C and relative humidity of ~25%) without encapsulation (Figure S18). Such stability tests suggest that ETL-free PV with CsFAMA perovskite films could be made with good stability during operation.

CONCLUSION

In conclusion, we use EQE to reveal that typical ETL-free perovskite PV with relatively low carrier lifetime exhibit more substantial photogenerated carrier loss compared with ETL-containing devices. PL quenching experiments show that the injection of carriers from the perovskite to the transparent conducting oxide contact (ITO) is less effective for ETL-free devices. To address this interface issue without changing the ETL-free design, we tailor the carrier lifetimes of the perovskite films and demonstrate that improved carrier lifetimes can enhance the carrier collection efficiency at the low-injection-rate interface, making the carrier dynamics in ETL-free devices essentially as good as those in ETL-containing devices. Based on such understanding, by using perovskite films with microsecond carrier lifetimes, ETL-free perovskite solar cells exhibit a best *PCE* of 19.52% with nearly-eliminated hysteresis and good stability. Such high-performance ETL-free perovskite solar cells are comparable to the analogous ETL-containing devices (*PCE*: 20.72%). These results offer new opportunities for versatile perovskite PV with simple processing, low cost and high performance. Our results also provide a general approach to improve the performance of PV with low-injection-rate interfaces, not only limited to the perovskite PV family.

EXPERIMENTAL PROCEDURES

Perovskite Film Deposition

For deposition of the pristine $MAPbI_3$ films, precursor solutions were prepared with 1.2 M PbI_2 and 1.2 M MAI in the DMF/DMSO co-solvent (V_{DMF}:V_{DMSO} = 9:1). Extra PbI_2 with levels of 0%, 2.5%, 5% and 7.5% (mol%, relative to stoichiometric $MAPbI_3$) was added into the $MAPbI_3$ precursor solutions, respectively, to tune the carrier lifetimes in the $MAPbI_3$ films. For each system, the precursor solutions were stirred at ~25 °C for 24 hours and filtered with a 0.45 μm PTFE syringe filter before further use. The $MAPbI_3$ films were then deposited by spin-coating the precursor solution using a spin speed of 5000 r.p.m for 30 s. 1.5 mL chlorobenzene was poured on the surface of the $MAPbI_3$ film ~5 s after commencing spin-coating. The as-deposited $MAPbI_3$ films were annealed at 100 °C for 10 min to form the resultant films. For the $Cs_{0.05}FA_{0.80}MA_{0.15}PbI_{2.55}Br_{0.45}$ (CsFAMA) films, a 1.2 M precursor solution was prepared with 0.06 M CsI, 0.96 M FAI, 0.18 M MABr, 1.02 M PbI_2 and 0.18 M $PbBr_2$ dissolved in DMF/DMSO co-solvent (V_{DMF}:V_{DMSO} = 4:1) and 10% extra PbI_2 (mol%, relative to CsFAMA) was added to the CsFAMA precursor solution.[7; 34] The precursor solution was stirred at ~25 °C for 24 hours and filtered with a 0.45 μm PTFE syringe filter before further use. To obtain the CsFAMA film, the CsFAMA precursor solution was spin-coated on the substrates (glass, glass/ITO or glass/ITO/SnO_2) using a spin speed of 2000 r.p.m for 10 s and 4000 r.p.m for 20 s. During the second spinning step, 1.5 mL of chlorobenzene was poured on the top surface of the CsFAMA film ~5 s before the end of the spinning cycle. Then, the as-deposited films were annealed on a hotplate at 100 °C for 10 min to form the resultant CsFAMA films. All the preparation and deposition steps were performed in a nitrogen-filled glovebox.

Device Fabrications

ITO-coated glass substrates (10 ohm/sq) were cleaned in soapy water, deionized water, acetone and isopropanol with sonication. The ITO-coated glass substrates were then subjected to ultraviolet-ozone (UVO) treatment for 10 min. For the ETL-free perovskite solar cells, the perovskite films were directly deposited on the ITO substrates by following the procedure mentioned above. Then, Li-doped Spiro-OMeTAD was spin-coated as the HTL on the perovskite films. A solution consisting of 72.5 mg Spiro-OMeTAD, 28.8 μL 4-tert-butylpyridine, 17.6 μL Li-bis(trifluoromethanesulfonyl)imide (Li-TFSI) solution (520 mg Li-TFSI in 1 mL acetonitrile) and 1 mL chlorobenzene was employed with a spin speed of 3000 r.p.m for 30s. To complete the device, Au was thermally evaporated on the HTL to serve as the electrode. For the devices with SnO_2 ETLs, the SnO_2 ETLs were deposited by spin-coating a SnO_2 suspension (15 wt.% in H_2O) in air on the UVO-treated ITO substrates and then annealing on a hotplate at 150 °C for 20 min to form ~20-nm-thick ETLs in air.[30] Then, the glass/ITO/SnO_2 substrates were treated with UVO for 10 min. Finally, the perovskite layer, Li-doped Spiro-

OMeTAD and Au were sequentially deposited to complete the ETL-containing perovskite solar cells, by following the procedures described above for the ETL-free devices.

Characterizations

Morphologies of the CsFAMA and $MAPbI_3$ films were imaged with a scanning electron microscope (SEM, FEI XL30 SEM-FEG). Atomic force microscopy (AFM) images were characterized using a scanning probe microscope (Digital Instruments Dimension 3100). X-ray diffraction (XRD) measurements were carried out on a PANalytical Empyrean Powder X-ray diffractometer using CuKα radiation. The charge carrier lifetimes were characterized via time-resolved photoluminescence (TRPL) experiments using an Edinburgh FLS980 fluorescence spectrometer with excitation wavelength of 510 nm. The steady-state PL was also measured with the Edinburgh FLS980 fluorescence spectrometer with excitation wavelength of 510 nm. Optical absorption measurements were performed on a Shimadzu UV-3600 spectrophotometer. The external quantum efficiency (EQE) was taken using a QE-R instrument from Enlitech without bias voltage. The current density-voltage (*J-V*) characteristics and steady-state output were measured using a Keithley 2420 source meter. The illumination source was a Newport Oriel 92192 solar simulator with an AM1.5G filter, operating at 100 mW cm^{-2}. All devices were masked with area of 0.09 cm^2 aperture to define the active areas. All the *J-V* characteristics of perovskite solar cells were evaluated with voltage scanning speed of 1.0 V/s. A standard silicon solar cell from Newport Corp. was used as a reference for *J-V* and EQE measurements. All measurements were performed under ambient conditions with relative humidity level below 30%.

DATA AND SOFTWARE AVAILABILITY

The accession number for the [data or structure] reported in this paper is [database abbreviation]: [accession number].

SUPPLEMENTAL INFORMATION

Supplemental Information includes 18 figures.

ACKNOWLEDGMENTS

This work was supported by National Natural Science Foundation of China (21573249) and the Strategic Priority Research Program of the Chinese Academy of Sciences (XDB12020100). Q.H., T.L. and D.B.M. acknowledge support by the National Science Foundation under Grant No. 1709294. Y.B. and M.J.T. acknowledge support from the Division of Chemical Sciences, Geosciences, and Biosciences, Office of Basic Energy Sciences, of the US Department of Energy through Grant DE-SC0001517. Any opinions, findings, conclusions or recommendations expressed in this work are those of the author(s) and do not necessarily reflect the views of the National Natural Science Foundation of China, Strategic Priority Research Program of the Chinese Academy of Sciences or the U. S. National Science Foundation.

AUTHOR CONTRIBUTIONS

Q.H. conceived the project. Q.H. and J.D. carried out the film deposition and device fabrication. Q.H. carried out the characterizations including SEM, XRD, PL and J-V, and analyzed data. Y.B. analyzed the TRPL data. T.L. performed UV-Vis measurement. J.M. conducted the AFM test and Y.Z. processed the AFM results and extracted roughness. Y.C. and Q.G. assisted in the Au electrode deposition. J.L. and J.C. assisted in XRD measurements. All authors discussed the results and commented on the manuscript. J. Liu and D.M. and J.H. supervised the project.

DECLARATION OF INTERESTS

The authors declare no competing interests.

REFERENCES AND NOTES

1. Kojima, A., Teshima, K., Shirai, Y., and Miyasaka, T. (2009). Organometal halide perovskites as visible-light sensitizers for photovoltaic cells. J. Am. Chem. Soc. *131*, 6050-6051.

2. Kim, H.-S., Lee, C.-R., Im, J.-H., Lee, K.-B., Moehl, T., Marchioro, A., Moon, S.-J., Humphry-Baker, R., Yum, J.-H., Moser, J.E., Grätzel, M., and Park, N.-G. (2012). Lead iodide perovskite sensitized all-solid-state submicron thin film mesoscopic solar cell with efficiency exceeding 9%. Sci. Rep. *2*, 591.

3. Jeon, N.J., Noh, J.H., Kim, Y.C., Yang, W.S., Ryu, S., and Seok, S.I. (2014). Solvent engineering for high-performance inorganic–organic hybrid perovskite solar cells. Nat. Mater. *13*, 897-903.
4. Zhou, H., Chen, Q., Li, G., Luo, S., Song, T.-b., Duan, H.-S., Hong, Z., You, J., Liu, Y., and Yang, Y. (2014). Interface engineering of highly efficient perovskite solar cells. Science *345*, 542-546.
5. Yang, W.S., Noh, J.H., Jeon, N.J., Kim, Y.C., Ryu, S., Seo, J., and Seok, S.I. (2015). High-performance photovoltaic perovskite layers fabricated through intramolecular exchange. Science *348*, 1234-1237.
6. Son, D.-Y., Lee, J.-W., Choi, Y.J., Jang, I.-H., Lee, S., Yoo, P.J., Shin, H., Ahn, N., Choi, M., Kim, D., and Park, N.-G. (2016). Self-formed grain boundary healing layer for highly efficient $CH_3NH_3PbI_3$ perovskite solar cells. Nat. Energy *1*, 16081.
7. Saliba, M., Matsui, T., Seo, J.-Y., Domanski, K., Correa-Baena, J.-P., Nazeeruddin, M.K., Zakeeruddin, S.M., Tress, W., Abate, A., Hagfeldt, A., and Grätzel, M. (2016). Cesium-containing triple cation perovskite solar cells: improved stability, reproducibility and high efficiency. Energy Environ. Sci. *9*, 1989-1997.
8. NREL efficiency chart. https://www.nrel.gov/pv/assets/images/efficiency-chart.png.
9. Yang, G., Tao, H., Qin, P., Ke, W., and Fang, G. (2016). Recent progress in electron transport layers for efficient perovskite solar cells. J. Mater. Chem. A *4*, 3970-3990.
10. Ke, W., Xiao, C., Wang, C., Saparov, B., Duan, H.-S., Zhao, D., Xiao, Z., Schulz, P., Harvey, S.P., Liao, W., Meng, W., Yu, Y., Cimaroli, A.J., Jiang, C.-S., Zhu, K., Al-Jassim, M., Fang, G., Mitzi, D.B., and Yan, Y. (2016). Employing lead thiocyanate additive to reduce the hysteresis and boost the fill factor of planar perovskite solar cells. Adv. Mater. *28*, 5214-5221.
11. Si, H., Liao, Q., Zhang, Z., Li, Y., Yang, X., Zhang, G., Kang, Z., and Zhang, Y. (2016). An innovative design of perovskite solar cells with Al_2O_3 inserting at ZnO/perovskite interface for improving the performance and stability. Nano Energy *22*, 223-231.
12. Shin, S.S., Yeom, E.J., Yang, W.S., Hur, S., Kim, M.G., Im, J., Seo, J., Noh, J.H., and Seok, S.I. (2017). Colloidally prepared La-doped $BaSnO_3$ electrodes for efficient, photostable perovskite solar cells. Science *356*, 167-171.
13. Han, Q., Bai, Y., Liu, J., Du, K.-z., Li, T., Ji, D., Zhou, Y., Cao, C., Shin, D., and Ding, J. (2017). Additive engineering for high-performance room-temperature-processed perovskite absorbers with micron-size grains and microsecond-range carrier lifetimes. Energy Environ. Sci. *10*, 2365-2371.
14. Wei, D., Wang, T., Ji, J., Li, M., Cui, P., Li, Y., Li, G., Mbengue, J.M., and Song, D. (2016). Photo-induced degradation of lead halide perovskite solar cells caused by the hole transport layer/metal electrode interface. J. Mater. Chem. A *4*, 1991-1998.
15. Yang, J., Siempelkamp, B.D., Mosconi, E., De Angelis, F., and Kelly, T.L. (2015). Origin of the thermal instability in $CH_3NH_3PbI_3$ thin films deposited on ZnO. Chem. Mater. *27*, 4229-4236.
16. Roose, B., Baena, J.-P.C., Gödel, K.C., Graetzel, M., Hagfeldt, A., Steiner, U., and Abate, A. (2016). Mesoporous SnO_2 electron selective contact enables UV-stable perovskite solar cells. Nano Energy *30*, 517-522.
17. Christians, J.A., Schulz, P., Tinkham, J.S., Schloemer, T.H., Harvey, S.P., de Villers, B.J.T., Sellinger, A., Berry, J.J., and Luther, J.M. (2018). Tailored interfaces of unencapsulated perovskite solar cells for >1,000 hour operational stability. Nat. Energy *3*, 68-74.
18. D'innocenzo, V., Grancini, G., Alcocer, M.J.P., Kandada, A.R.S., Stranks, S.D., Lee, M.M., Lanzani, G., Snaith, H.J., and Petrozza, A. (2014). Excitons versus free charges in organo-lead tri-halide perovskites. Nat. Commun. *5*, 3586.
19. Stranks, S.D., Eperon, G.E., Grancini, G., Menelaou, C., Alcocer, M.J., Leijtens, T., Herz, L.M., Petrozza, A., and Snaith, H.J. (2013). Electron-hole diffusion lengths exceeding 1 micrometer in an organometal trihalide perovskite absorber. Science *342*, 341-344.
20. Xing, G., Mathews, N., Sun, S., Lim, S.S., Lam, Y.M., Grätzel, M., Mhaisalkar, S., and Sum, T.C. (2013). Long-range balanced electron-and hole-transport lengths in organic-inorganic $CH_3NH_3PbI_3$. Science *342*, 344-347.
21. Liu, D., Yang, J., and Kelly, T.L. (2014). Compact Layer Free Perovskite Solar Cells with 13.5% Efficiency. J. Am. Chem. Soc. *136*, 17116-17122.
22. Ke, W., Fang, G., Wan, J., Tao, H., Liu, Q., Xiong, L., Qin, P., Wang, J., Lei, H., Yang, G., Qin, M., Zhao, X., and Yan, Y. (2015). Efficient hole-blocking layer-free planar halide perovskite thin-film solar cells. Nat. Commun. *6*, 6700.
23. Zhu, Q., Bao, X., Yu, J., Zhu, D., Qiu, M., Yang, R., and Dong, L. (2016). Compact Layer Free Perovskite Solar Cells with a High-Mobility Hole-Transporting Layer. ACS Appl. Mater. Interfaces *8*, 2652-2657.
24. Huang, L., Xu, J., Sun, X., Du, Y., Cai, H., Ni, J., Li, J., Hu, Z., and Zhang, J. (2016). Toward Revealing the Critical Role of Perovskite Coverage in Highly Efficient Electron-Transport Layer-Free Perovskite Solar Cells: An Energy Band and Equivalent Circuit Model Perspective. ACS Appl. Mater. Interfaces *8*, 9811-9820.
25. Pascual, J., Kosta, I., Tuyen Ngo, T., Chuvilin, A., Cabanero, G., Grande, H.J., Barea, E.M., Mora-SerÓ, I., Delgado, J.L., and Tena-Zaera, R. (2016). Electron Transport Layer-Free Solar Cells Based on Perovskite–Fullerene Blend Films with Enhanced Performance and Stability. ChemSusChem *9*, 2679-2685.
26. Xu, X., Chen, Q., Hong, Z., Zhou, H., Liu, Z., Chang, W.-H., Sun, P., Chen, H., Marco, N.D., and Wang, M. (2015). Working mechanism for flexible perovskite solar cells with simplified architecture. Nano Lett. *15*, 6514-6520.
27. Zhang, Y., Liu, M., Eperon, G.E., Leijtens, T.C., McMeekin, D., Saliba, M., Zhang, W., de Bastiani, M., Petrozza, A., and Herz, L.M. (2015). Charge selective contacts, mobile ions and anomalous hysteresis in organic–inorganic perovskite solar cells. Mater. Horiz. *2*, 315-322.
28. Huang, L., Hu, Z., Xu, J., Sun, X., Du, Y., Ni, J., Cai, H., Li, J., and Zhang, J. (2016). Efficient planar perovskite solar cells without a high temperature processed titanium dioxide electron transport layer. Sol. Energy Mater. Sol. Cells *149*, 1-8.
29. Zheng, E., Wang, X.-F., Song, J., Yan, L., Tian, W., and Miyasaka, T. (2015). PbI_2-based dipping-controlled material conversion for compact layer free perovskite solar cells. ACS Appl. Mater. Interfaces *7*, 18156-18162.
30. Jiang, Q., Zhang, L., Wang, H., Yang, X., Meng, J., Liu, H., Yin, Z., Wu, J., Zhang, X., and You, J. (2016). Enhanced electron extraction using SnO_2 for high-efficiency planar-structure $HC(NH_2)_2PbI_3$-based perovskite solar cells. Nat. Energy *2*, 16177.

31. Wu, W.-Q., Wang, Q., Fang, Y., Shao, Y., Tang, S., Deng, Y., Lu, H., Liu, Y., Li, T., Yang, Z., Gruverman, A., and Huang, J. (2018). Molecular doping enabled scalable blading of efficient hole-transport-layer-free perovskite solar cells. Nat. Commun. *9*, 1625.

32. Chen, Q., Zhou, H., Song, T.-B., Luo, S., Hong, Z., Duan, H.-S., Dou, L., Liu, Y., and Yang, Y. (2014). Controllable self-induced passivation of hybrid lead iodide perovskites toward high performance solar cells. Nano Lett. *14*, 4158-4163.

33. Rehman, W., McMeekin, D.P., Patel, J.B., Milot, R.L., Johnston, M.B., Snaith, H.J., and Herz, L.M. (2017). Photovoltaic mixed-cation lead mixed-halide perovskites: links between crystallinity, photo-stability and electronic properties. Energy Environ. Sci. *10*, 361-369.

34. Giordano, F., Abate, A., Baena, J.P.C., Saliba, M., Matsui, T., Im, S.H., Zakeeruddin, S.M., Nazeeruddin, M.K., Hagfeldt, A., and Graetzel, M. (2016). Enhanced electronic properties in mesoporous TiO_2 via lithium doping for high-efficiency perovskite solar cells. Nat. Commun. *7*, 10379.